SOME ASPECTS OF THE PERFORMANCE OF A BASIC VERSION OF THE LMD GENERAL CIRCULATION MODEL IN JANUARY AND JULY SIMULATIONS

R. Sadourny
Laboratoire de Météorologie Dynamique
75231 Paris Cedex 05

1. DESCRIPTION OF THE MODEL

The simulations described here were performed using a version of the LMD model which was the standard one during spring 1982. The description of the model has not yet been published, except for a brief LMD Internal Report (Fouquart, Laval and Sadourny, 1978). Therefore we begin by a schematic survey of its basic features,

Coordinates : λ, $\mu = \sin\varphi$, $\sigma = f(p/p_s)$.

Pronostic variables : p_s, u, v, θ, q.

Grid : Arakawa's C-grid, uniform in longitude and sine of latitude with poles at meridional velocity location. Resolution : 64 points in longitude, 50 points in latitude, 11 layers (See figure 1 for more details).

Numerical scheme : Finite-differences with longitudinal filtering near the poles for the gradient and divergence operators. Potential enstrophy conserved exactly for divergent barotropic flow. Energy conserved for irrotational adiabatic flow. θ and θ^2 exactly conserved for adiabatic flow (See Sadourny 1975 a, 1975 b, 1980).

Lateral diffusion : linear. Bilaplacian for the rotational part of the wind and potential temperature, Laplacian for the divergent part of the wind, all on sigma-surfaces. Upstream flux form for horizontal transport of moisture.

Vertical diffusion : In the four lowermost layers, vertical diffusion coefficient depending on stability and wind shear. In the free atmosphere, "minimum" diffusion of moisture to ensure strict positivity of the mixing ratio.

Convection : Dry convective adjustment. Moist convective adjustment (Manabe and Strickler, 1964) over saturated profiles. Kuo's (1974) scheme over unsaturated layers (See Laval, Le Treut and Sadourny, 1981).

Radiation : Long wave : modification of Katayama (1972).

Solar : Fouquart et Bonnel, 1980.

The version used here has non interactive, zonally averaged clouds.

Land surface processes : Prognostic equations for temperature and moisture. (See Laval, Sadourny and Serafini, 1981). Fixed temperatures for oceans.

2. DESCRIPTION OF THE EXPERIMENTS

The two experiments described here are 57 day- January and July simulations, both starting from real conditions. These initial conditions were interpolated from ECMWF's FGGE III-B analyses corresponding to 21 January 1979 and 11 June 1979 respectively. The first seven days of each simulation were used in the WGNE forecast intercomparison experiment (1982). Only statistics concerning the last 30 days are presented here. The boundary conditions were specified as follows :

Topography : Mesh-averaged RAND 1° x 1° data (See figure 2)

Sea surface temperature : Mesh-averaged RAND January and July 1° x 1° data

Albedo : Independent of snow cover. Mesh-averaged 10° x 10° data from Bartman (1980) with corrections for land-sea contrast.(figures 3,4).

Sea Ice boundary : from RAND 1° x 1° data.

Sun declination : constant, mid-January and mid-June values.

3. STATISTICS : CHARTS

3.1. Sea level pressure

3.1.1. January mean (figure 5)

In the Southern hemisphere, the thermal lows over the continents are well developed, but the high pressure centres above the subtropical oceans are weaker than normally observed. In midlatitudes, the meridional gradient has about a realistic value ; but the subarctic low-pressure belt is weaker than observed and displaced northward by at least 5 degrees. (Note that the meridional resolution of the model is rather coarse at high latitudes : the first row of gridpoints is located around 78°S, the second row at about 70°S, the fourth row in the vicinity of 60°S).

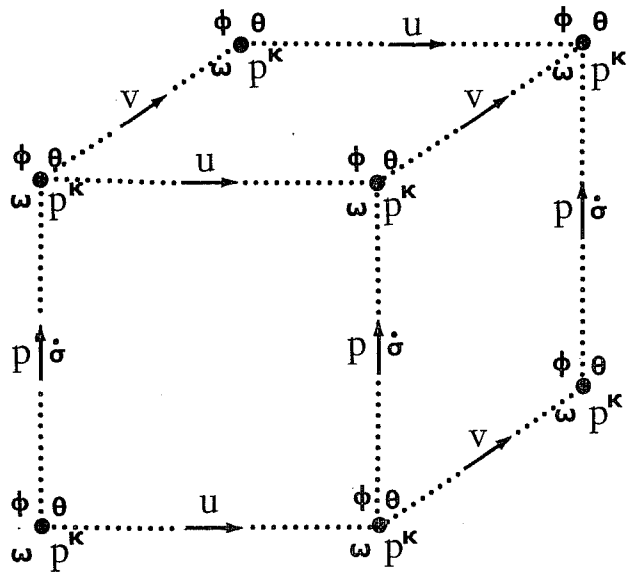

Fig. 1 Grid specifications.

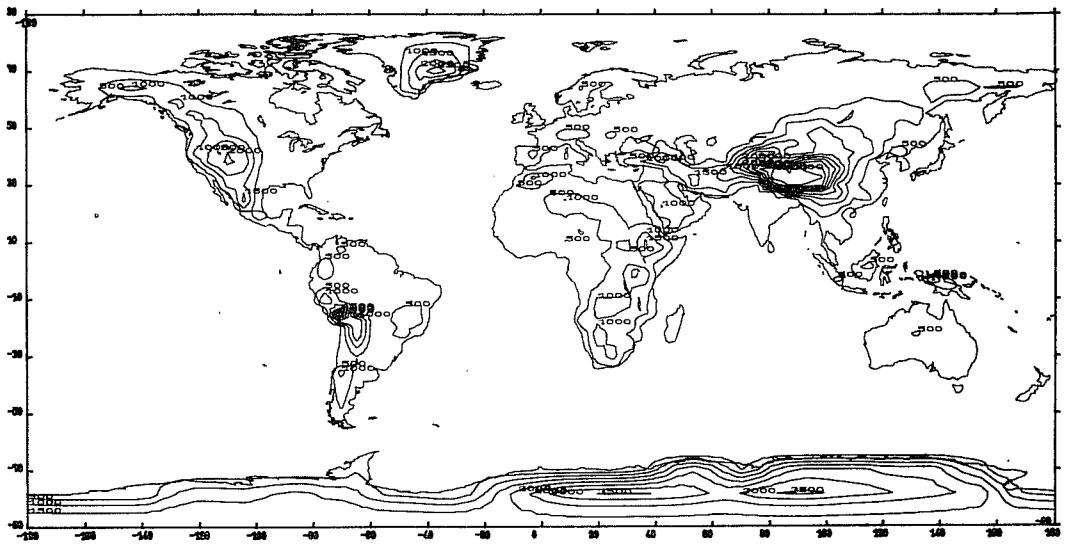

Fig. 2 Orography (spacing 500 metres).

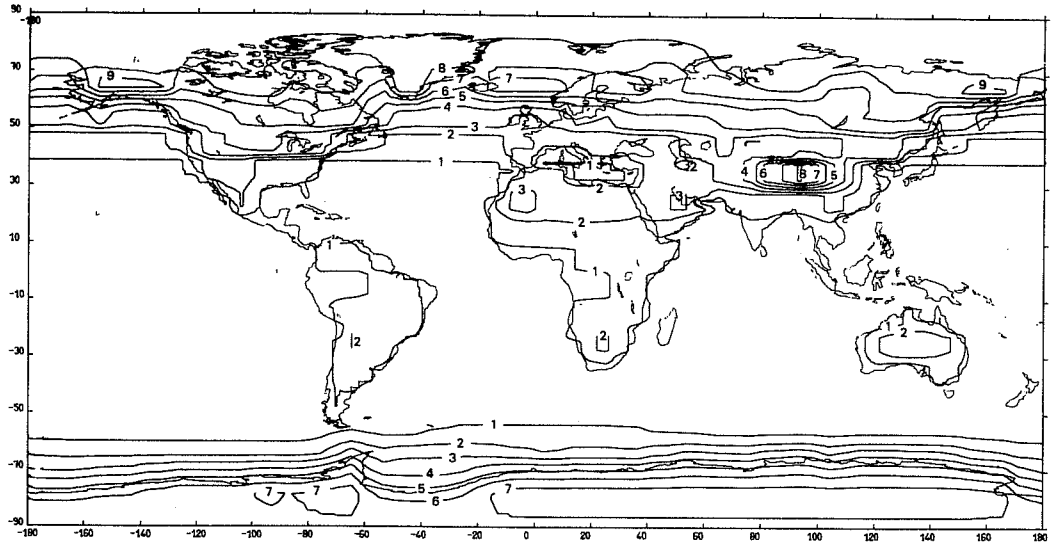

Fig. 3 Surface albedo for January (Bartman 1980) ; in tenths, spacing 1/10.

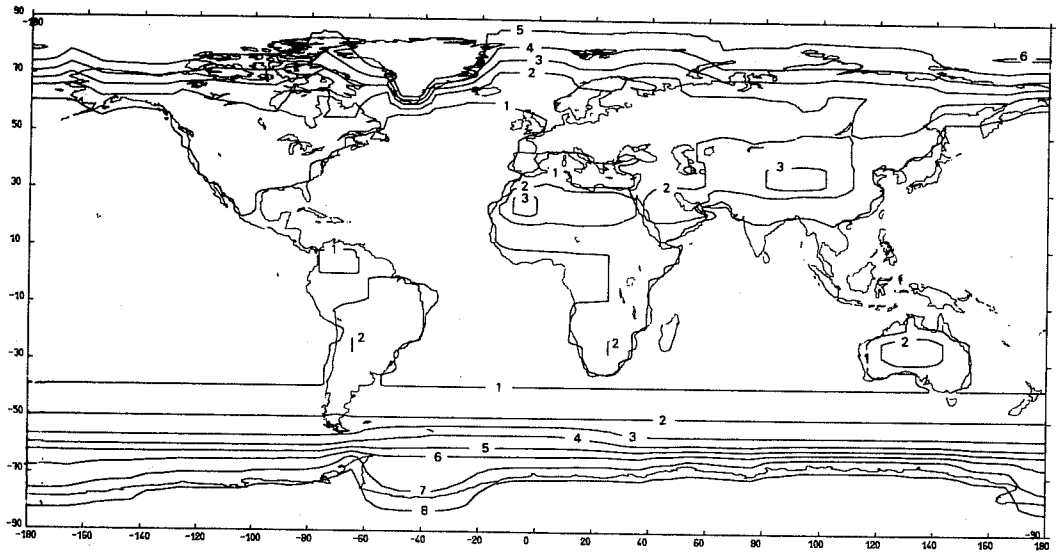

Fig. 4 Same as figure 3 but for July.

In the Northern Hemisphere, the Siberian high is weaker than observed ; especially weak is the high pressure ridge which normally links Eastern Siberia to Alaska above the Bering Straights. The situation produced by the model over Northern Pacific is somewhat interesting, as it has the characteristics of a blocking event, which prevailed during the second month of our integration : with a high pressure center oscillating around the Aleutian area, and weak lows making their way south of it towards the US coast. On the 57th day a low pressure system was finally restored over the gulf of Alaska. The Icelandic low has an eastward extension stronger than observed ; its southward extension is hindered by a strong high pressure center over Spain, which seems to be an almost permanent feature of the model's climate.

3.1.2. July mean (figure 6)

In July the thermal lows (especially the Monsoon low) are well developed over the Northern Hemisphere continents. The extension and strength of the oceanic high pressure centres is realistic, but the weak summer subarctic lows are underestimated. The general pattern in the Northern Hemisphere is more realistic than in January : of course the sea level pressure field is easier to model in summer, because it is more directly related to the geographical thermal contrasts ; in winter, complex mechanisms like baroclinic instability and orographic effects become more important and have to be modelled more accurately. The underestimation of subarctic summer lows in the present simulations points to possible weaknesses in our treatment of baroclinic instability, attributable in part to the lack in resolution. The Southern Hemisphere subarctic pressure belt is much stronger than in January, although it looks again somewhat shifted to the north.

3.1.3. Variance (figures 7,8)

The regions of large variance are the low pressure areas in the winter hemisphere ; they approximately follow the cyclone paths. Maximum values in January are realistic, but the variance over Northern Atlantic is unrealistically confined north of 50°, due to the standing high pressure centre over Spain. Over North Pacific, the variance in the Aleutian region is comparatively low, due to the blocking situation there. The variance in summer appears largely underestimated, which again may point to some deficiencies in the treatment of baroclinic instability ; also, the use of non-interactive, zonally-averaged clouds in the radiation budget is expected to reduce the variance level.

3.2. Geopotential height at 500 millibars

For both January (figure 9) and July (figure 10) the magnitude of the meridional gradients is realistic in both hemispheres. In the January case, one prominent feature is the pronounced ridge over the Aleutian area, consistent with the strong anomaly already observed there in the sea level pressure field. The amplitude of the planetary wave in the Northern Hemisphere summer is underestimated.

The variance of geopotential height at 500 millibars is shown on figure 11, for January, and figure 12, for July. In the Northern Hemisphere winter, the magnitude and location of maxima is realistic ; but the extension of the large variance areas (say, areas with more than 100m variance) is underestimated if we compare to Blackmon and Lau's (1980) observed values. Thus the hemispheric mean is also underestimated. And again the signature of the Aleutian anomaly is clearly visible on the January map.

3.3. Horizontal winds

Monthly-averaged horizontal winds at 200 millibars, 850 millibars and sea-level, for January and July, are displayed on figures 13 to 18. Conspicuous are the split jets in the upper troposphere, and the strong July easterlies over the Indian Ocean. Close to the equator, some two-grid interval noise can be detected in the 200 millibar fields : over the Indian Ocean in January, over Africa in July. This noise has a characteristic pattern of alternating meridional bands with positive and negative vorticity. It has its origin in the way vorticity and winds are averaged in the rotation term of the equation of motion (Sadourny, 1975 a,b) : the pattern observed here is a stationary solution of the discretised equations in the non rotating case. It appears therefore only near the equator and has apparently no serious deteriorating effect on the rest of the flow.

The monsoon regimes are prominent features of the wind velocity charts at 850 millibars. The Summer Monsoon over the Indian Ocean is reasonably strong, with winds in excess of 25 ms^{-1}. Abnormally strong westerlies are produced in January over Indonesia, inducing an extremely strong convergence over New-Guinea. These features are also visible on the sea-level charts, which clearly shows the Intertropical Convergence and the anticyclonic circulations over oceans in the subtropics.

The charts of velocity potential at 200 millibars (figure 19 and figure 20) essentially reflect the geographical upper structure of the monthly-averaged Hadley-Walker circulation. In January the three cells over Indonesia, Africa and Latin America are clearly visible, but the former is much stronger than the two others. The main divergence centre is located over New Guinea where we have

already noticed a strong low-level convergence. Apart from the weakness of the African and American cells, the order of magnitude seems realistic. In July the divergent circulation looks much too strong, and overwhelmingly dominated by wave number one.

3.4. Surface wind stress

Charts of monthly-averaged surface wind stress are shown on figures 21 (January) and 22 (July). The maximum wind stress in July occurs on the Somali ridge, with a magnitude of .5 Pa, which looks reasonable.

3.5. Surface air temperature

In January (figure 23), extremely cold temperatures below -40°C are obtained over North-Eastern Siberia and the North of Canada, in connection with the anomalous circulation pattern around the Aleutian area, while maximum temperatures slightly above 30°C occur in the Southern Hemisphere subtropics. In July (figure 24) temperatures in excess of 40°C are obtained in the Sahara, while Eastern Antarctica gets colder than -45°C.

3.6. Evaporation

Charts of evaporation are displayed on figures 25 and 26. In January, evaporation over the Gulf Stream area is markedly weaker than its counterpart over the Kuroshio region ; strong evaporation is also induced by the surface westerly flow over Indonesia ; while some areas with possibly unrealistic large values are noticeable on the west coasts of continents. In July, evaporation seems underestimated in the Southern part of the Indian Ocean, and overestimated in the Northern part, especially over the bay of Bengal, and over the China Sea.

3.7. Precipitations

A prominent feature of the precipitation charts displayed on figures 27 and 28, is the strong coupling of rainfall with orography. Rain over mountains may be artificially produced by cooling due to lateral diffusion of potential temperature along sigma surfaces. Lateral diffusion of moisture should be less of a problem, because diffusion due to upstream differencing actually follows the physical flow pattern.

In spite of the coarse resolution of the model, the ITCZ is fairly well resolved due to the choice of $\sin\varphi$ as meridional coordinate ; the mesh size at the equator is actually 562.5 km in the longitudinal direction, but 220 km only in the meridional direction. The well developed summer monsoon already observed in 3.3. brings the expected rainfall over India and South-East Asia, although in India, probably due to insufficient resolution of the land-sea contrast, the

rain does not extend far enough to the north. East of the China sea, a large patch of heavy rainfall (up to 4 cm day^{-1}) is observed in July, to be related to the excessive strength of the Hadley-Walker circulation.

In January, precipitation is heaviest on New Guinea ; also, the signature of the Aleutian anomaly is here again clearly visible, with precipitations on the West Coast of America significantly deviated south of their normal path.

3.8. Soil moisture

A dominant feature of the present scheme for ground hydrology is a marked tendency for producing sharp moisture contrasts, as can be seen on figures 29 and 30. Looking at those regions which are driest on both charts, we notice that the Atacama Desert, the Namibia Desert, the Australian Desert, the Sahara, the Desert of Thar and the Desert of Gobi are actually produced by the model. On the contrary, the model fails to capture the arid strip of Patagonia, because of its poor resolution of the barrier effect of the Andes and, consequently, of drying process normally implied there by vertical excursions of parcels.

4. STATISTICS : MERIDIONAL CROSS SECTIONS

4.1. Temperature

Monthly and zonally averaged temperatures are displayed on figures 31 and 32. The stratosphere is always too cold, with temperatures 10 to 15 K less than climatology in the equatorial belt ; the situation is even worse near the North Pole in wintertime, with temperatures 20 to 25 K less than climatology. The troposphere appears slightly too cold - one to two degrees - in January ; in July the contrast between summer and winter hemispheres is slightly exaggerated. Apart from these defects the latitudinal distribution is generally speaking realistic.

4.2. Zonal wind

Figure 33 shows the monthly and zonally averaged zonal velocity. As can be expected from the systematic errors already observed in the stratospheric temperature field, the subtropical westerly jet is partly absorbed by the stratospheric polar night jet ; it is therefore slightly displaced upwards and northwards. The magnitude of both westerly jets is about right or perhaps slightly weak. Tropical easterlies are realistically distributed but tend to vanish around 300 millibars ; in the lower troposphere conspicuous is the signature of the

north-east monsoon at 10 degrees north, and at 10 degrees south - the prevailing effect of the westerly jet over Indonesia, already mentioned in 3.3.

Zonal winds in July are described on figure 34. Again the winter hemisphere westerly jet is not closed as it should be, although its magnitude is about right. In the Northern Hemisphere, the summertime jet is unrealistically weak, the summer dynamics in the middle latitudes of the Northern Hemisphere are rather poorly simulated in the present experiment (weak jet, weak meridional temperature gradient, weak cyclogenesis). The tropical easterlies are realistic ; westerlies inbedded in the easterlies prevail at 10 degrees north due to the dominant features of the South-West Monsoon over the Northern Indian Ocean.

4.3. Meridional wind

Meridional cross-sections of the monthly-averaged meridional velocities are shown on figure 35 and 36. On both charts the winter and summer tropical Hadley cells, Ferrell cells and polar Hadley cells are clearly visible. The dominant Hadley cell is somewhat weaker than observed in January ; it seems slightly too strong in July, a feature consistent with the too intense velocity potential at 200 millibars observed on figure 20.

5. REFERENCES

Bartman, F.L., 1980 - A time variable model of the earth's albedo. Nasa Contractor Report 159259.

Blackmon, M.L. and N.C. Lau, 1980 - Regional characteristics of the Northern Hemisphere wintertime circulation : a comparison of the simulation of a GFDL general circulation model with observations. J. Atm. Sci., 37, 497-514.

Fouquart, Y., K. Laval et R. Sadourny, 1978 : The LMD general circulation model. Internal Report N° 86, Laboratoire de Météorologie Dynamique, Paris.

Katayama, A, 1972 - A simplified scheme for computing radiative transfer in the troposphere. Tech. Rep. N° 6, Dept of Meteorology, University of California, Los Angeles.

Kuo, H.L., 1965 - On the formation and intensification of tropical cyclones through latent heat release by cumulus convection, J. Atm. Sci., 22, 40-63.

Laval, K., H. Le Treut and R. Sadourny, 1981 - Effect of cumulus parameterization on the dynamics of a General Circulation Model. Geophys. Astrophys. Fluid Dynamics, 17, 113-127.

Laval K., R. Sadourny and Y. Serafini, 1981 - Land surface processes in a simplified general circulation model. Geophys. Astrophys. Fluid Dynamics, 17, 129-150.

Manabe, S., and R.F. Strickler, 1964 - On the thermal equilibrium of the atmosphere with convective adjustment. J. Atm. Sci., 21, 361-385.

Sadourny, R., 1975 a - The dynamics of finite-difference models of the shallow water equations. J. Atm. Sci., 32, 680-689.

Sadourny, R., 1975 b - Compressible model flows on the sphere. J. Atm. Sci., 32, 2103-2110.

Sadourny, R., 1980 - Conservation laws turbulence and numerical modeling of large-scale flows, 1979 ECMWF Seminar, Vol II.

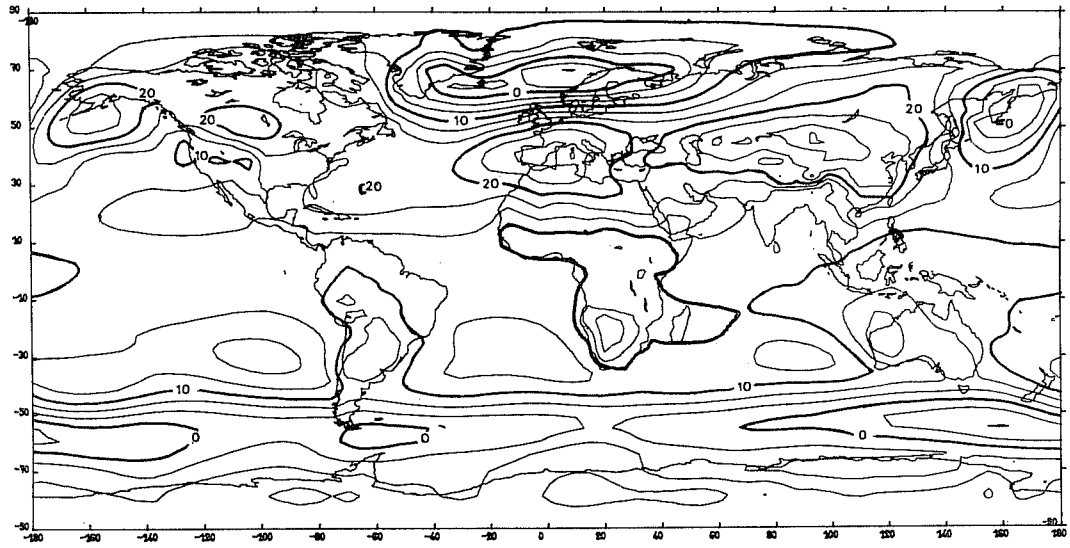

Fig. 5 Mean sea level pressure for January (in millibars ; spacing : 10/3 millibars).

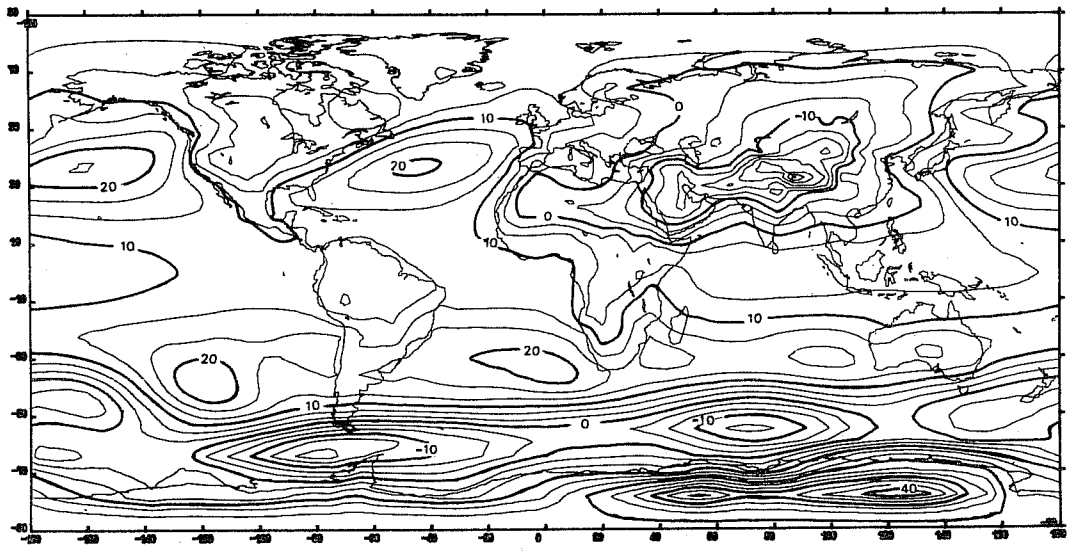

Fig. 6 Same as figure 5, but for July.

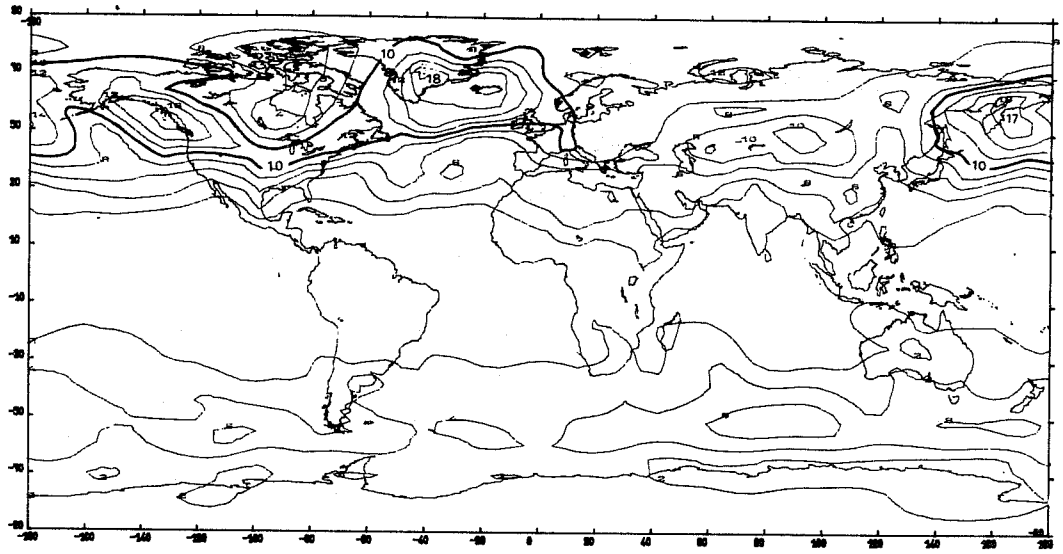

Fig. 7 Transient variance of sea level pressure for January (in millibars ; spacing 2 mb).

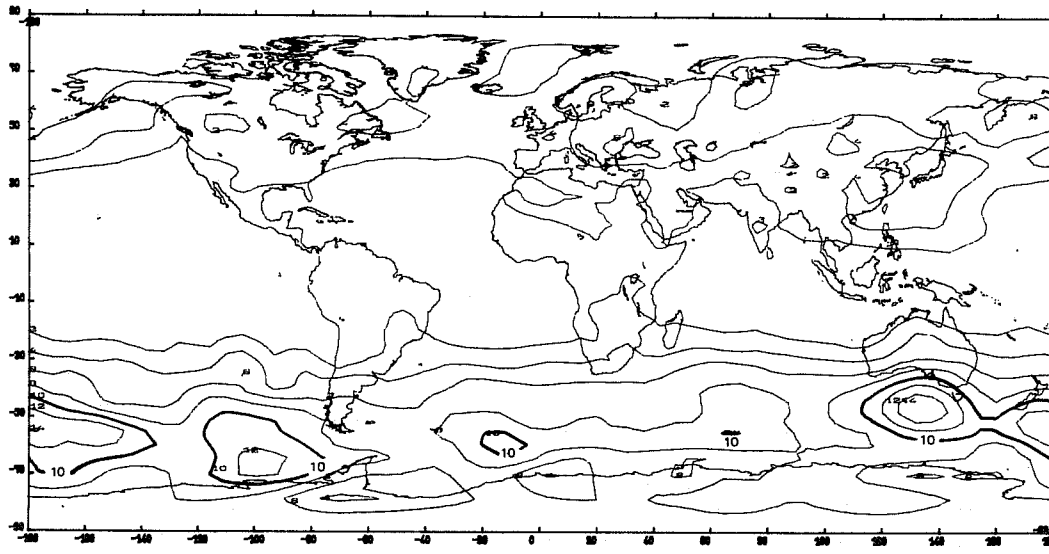

Fig. 8 Same as figure 7 but for July.

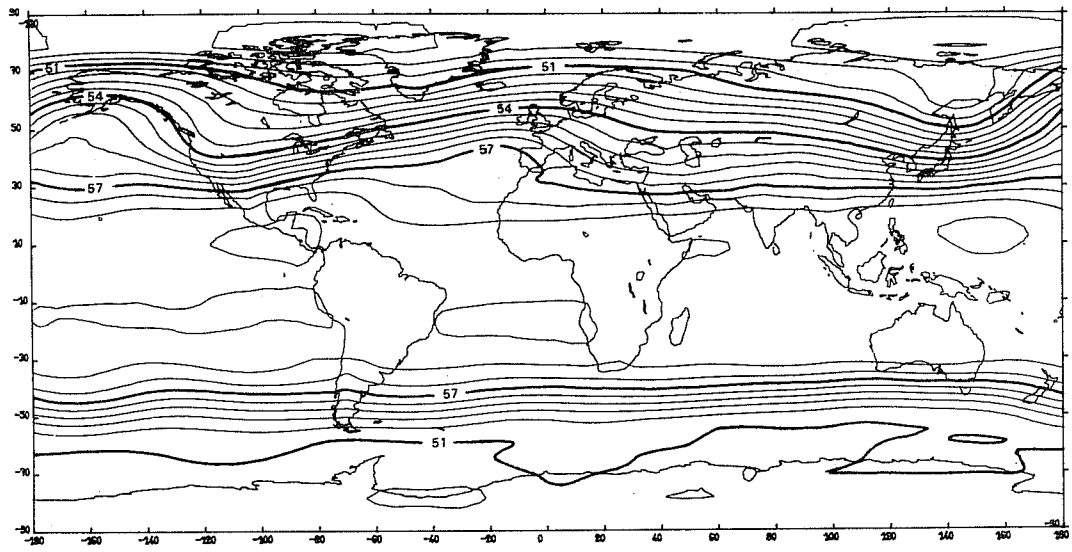

Fig. 9 Mean geopotential height at 500 millibars
for January (in hectometers ; spacing 60 m)

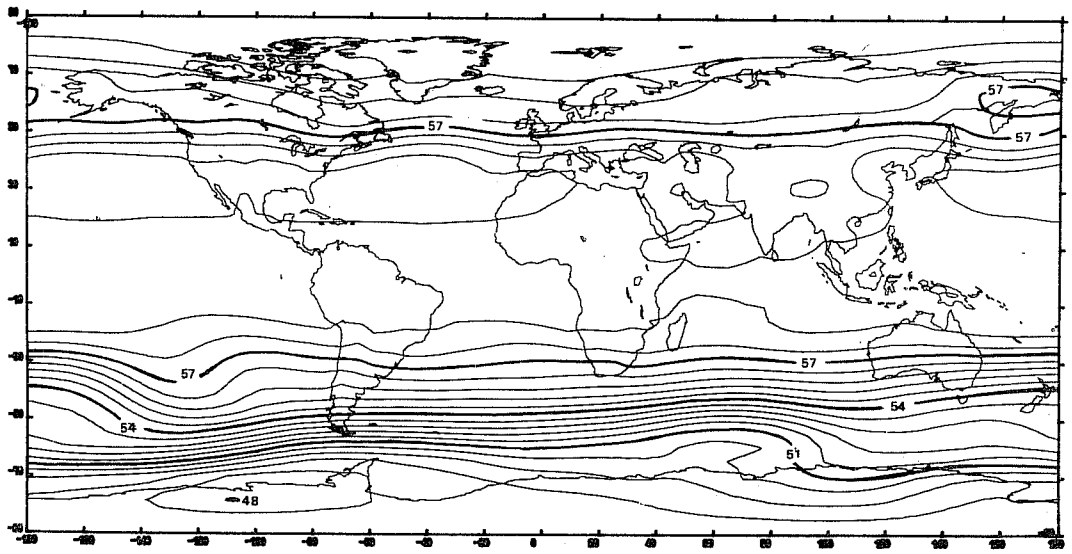

Fig. 10 Same as figure 9 but for July.

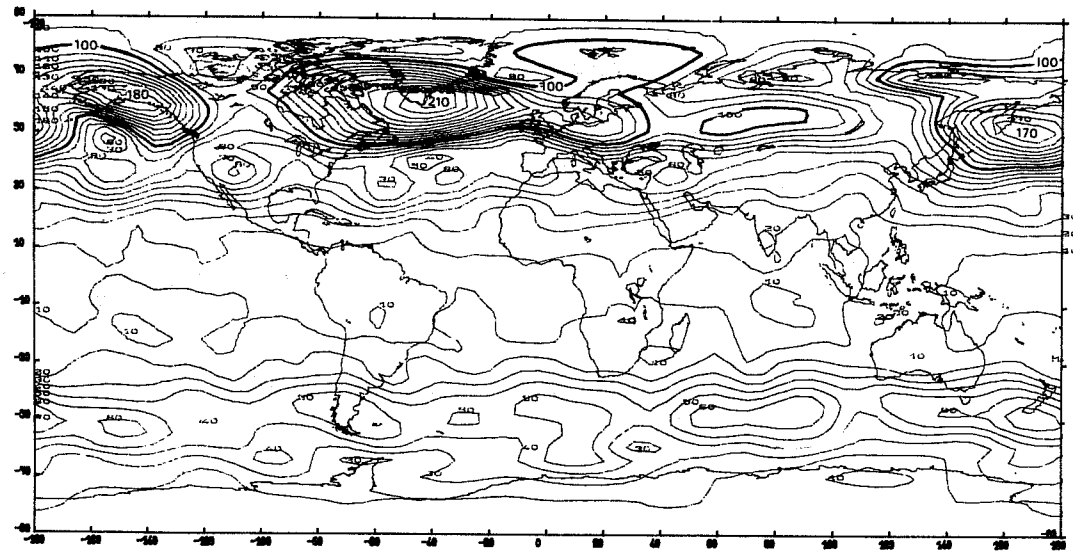

Fig. 11 Transient variance of geopotential height at 500 millibars in January (in meters ; spacing 10 meters).

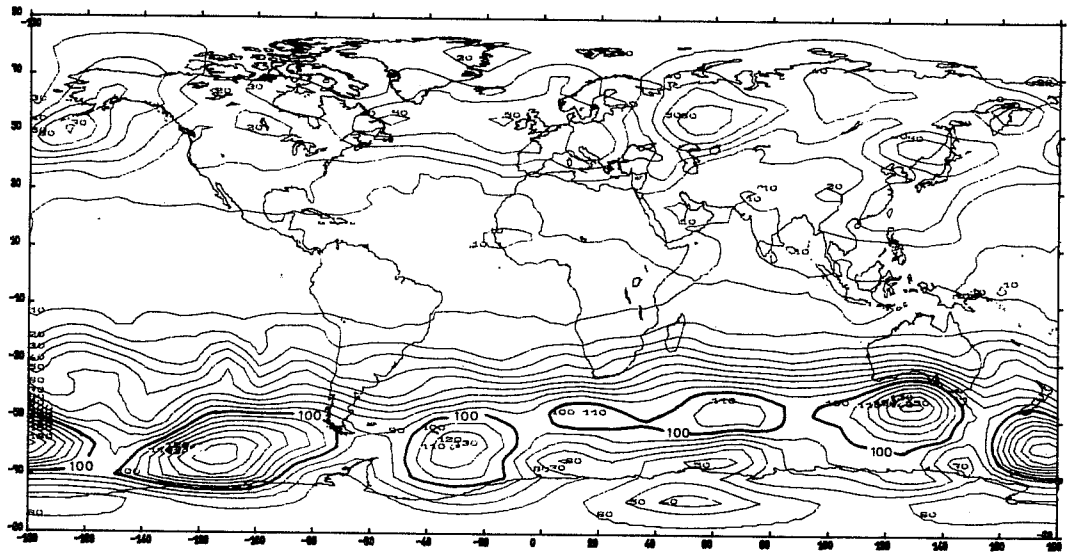

Fig. 12 Same as figure 11 but for July.

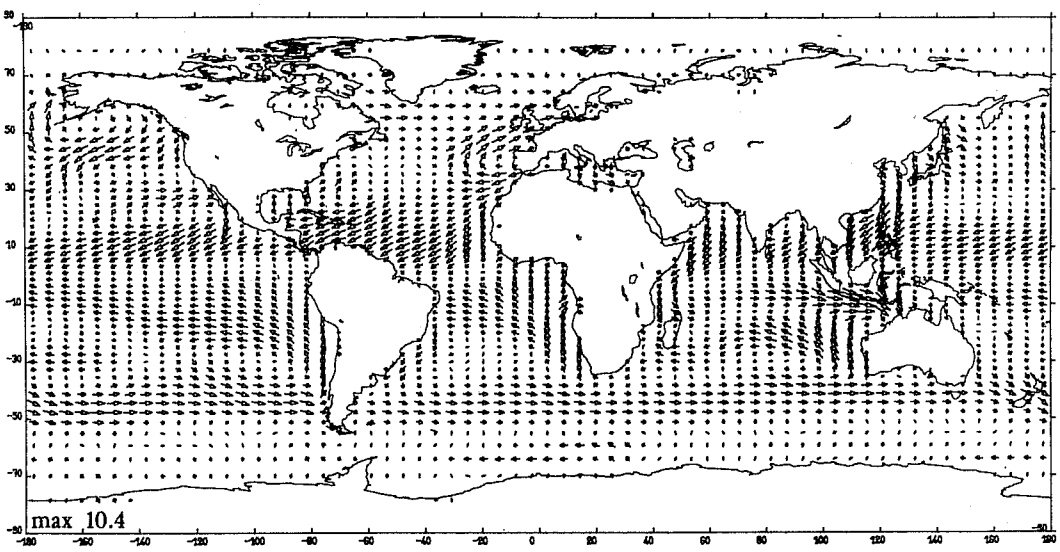

Fig. 13 Mean wind velocity at 200 millibars for January (maximum value in ms^{-1} at bottom left).

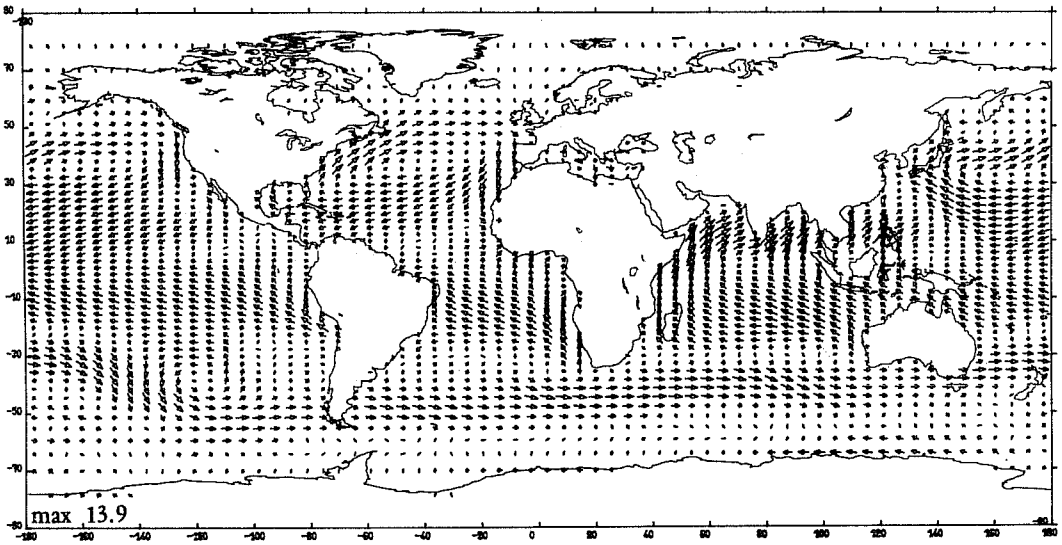

Fig. 14 Same as figure 13 but for July.

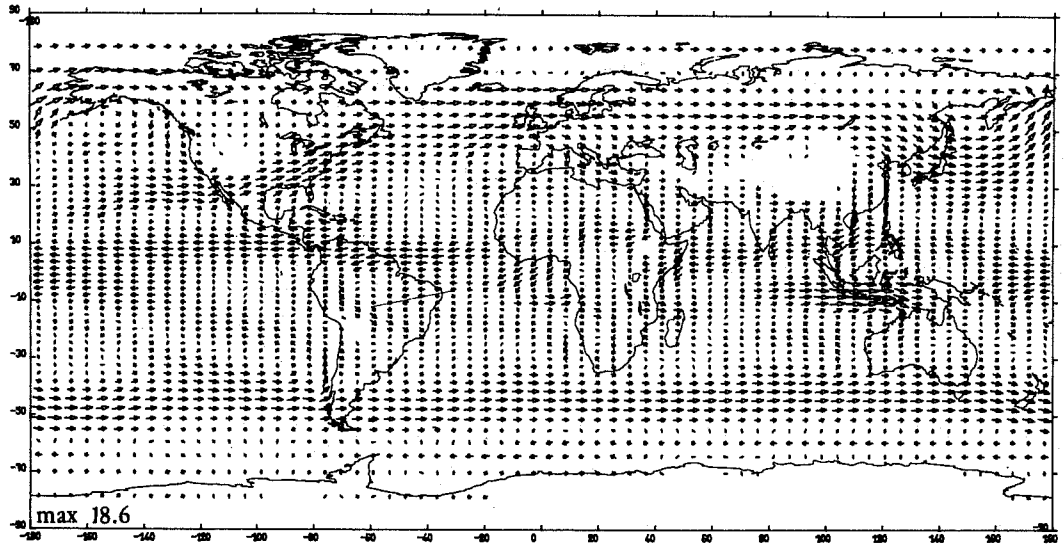

Fig. 15 Same as figure 13 but at 850 millibars.

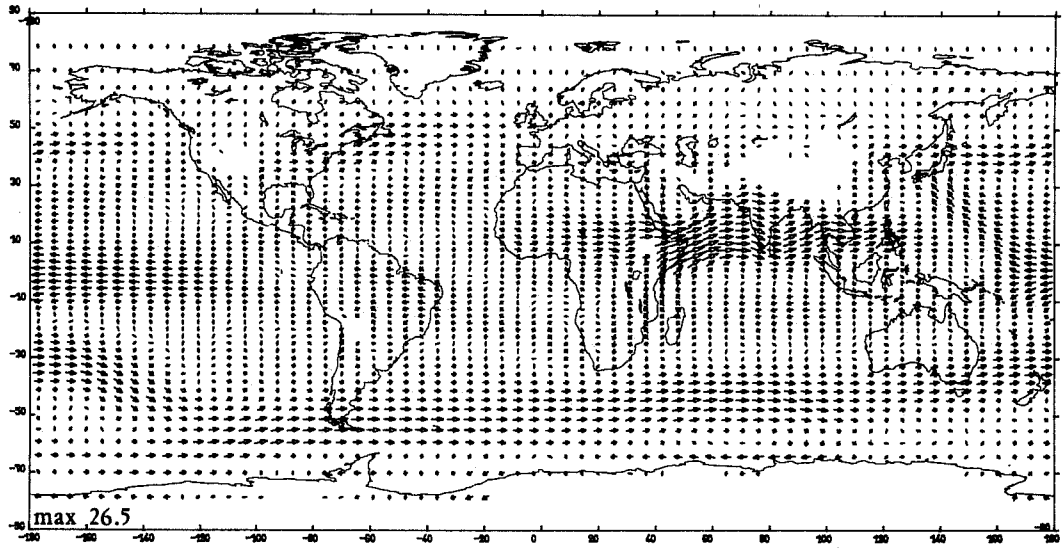

Fig. 16 Same as figure 15 but for July.

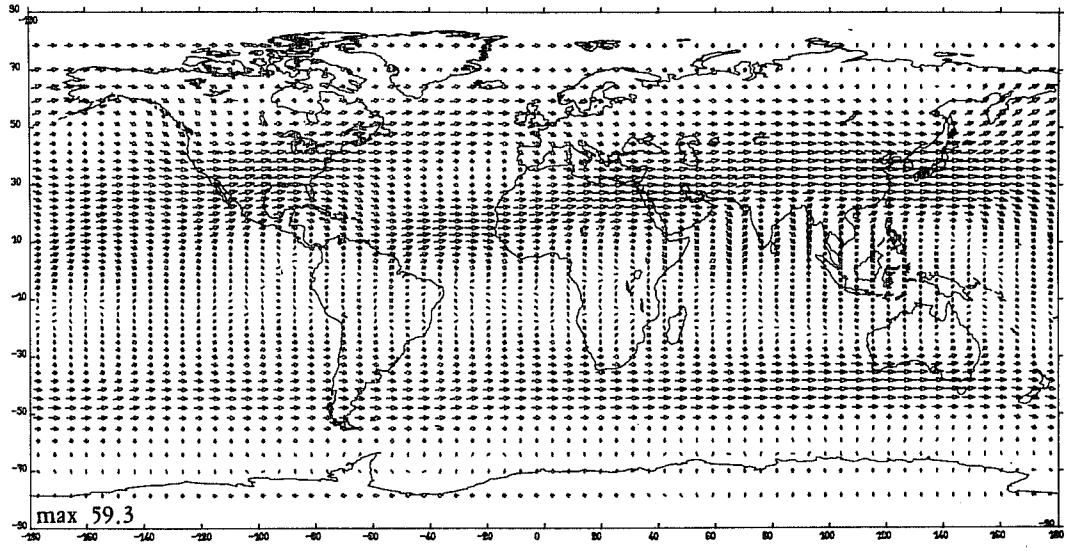

Fig. 17 Same as figure 13 but at sea level.

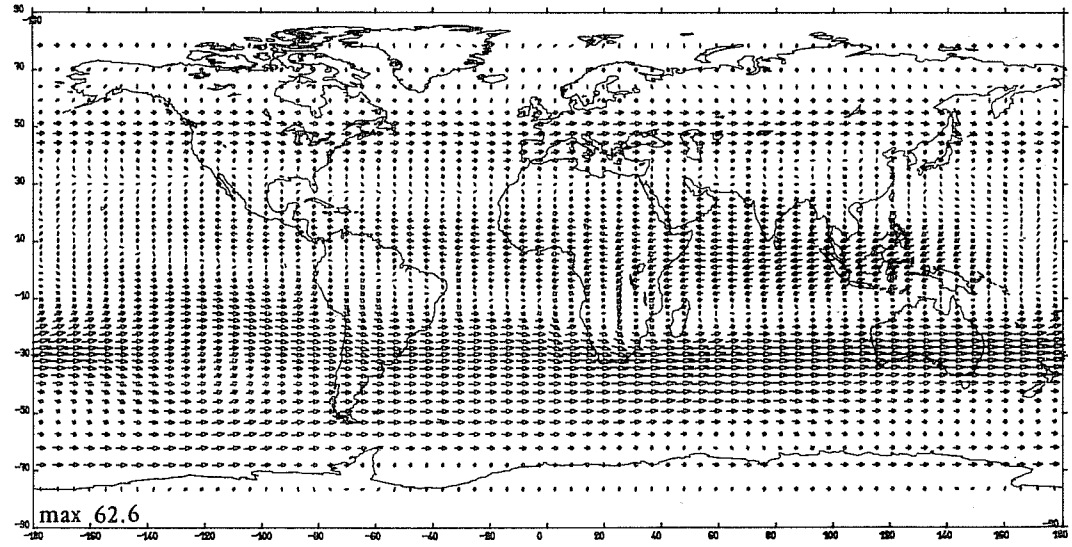

Fig. 18 Same as figure 17 but for July

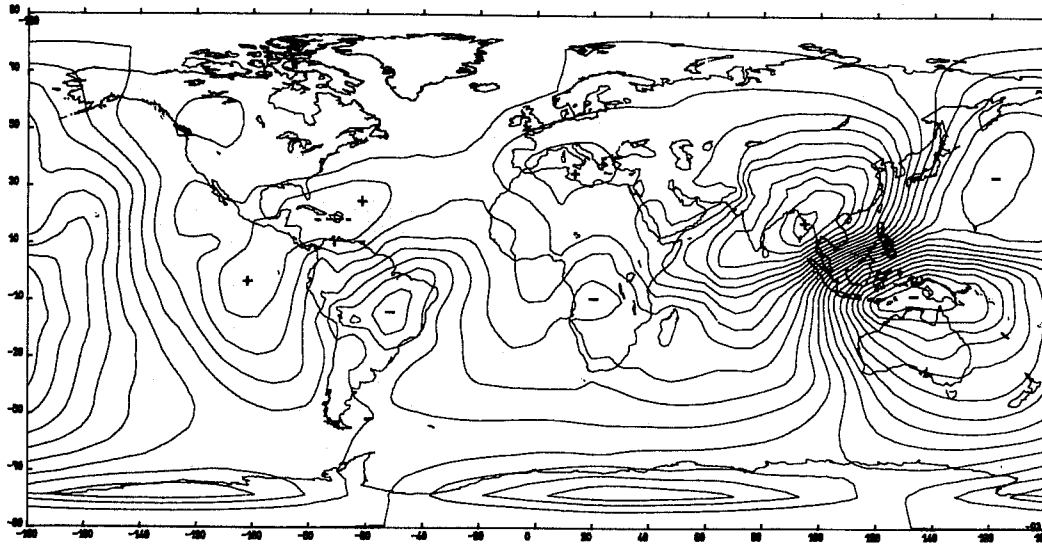

Fig. 19 Mean velocity potential at 200 millibars for January. Spacing 1 m^2 s^{-1}.

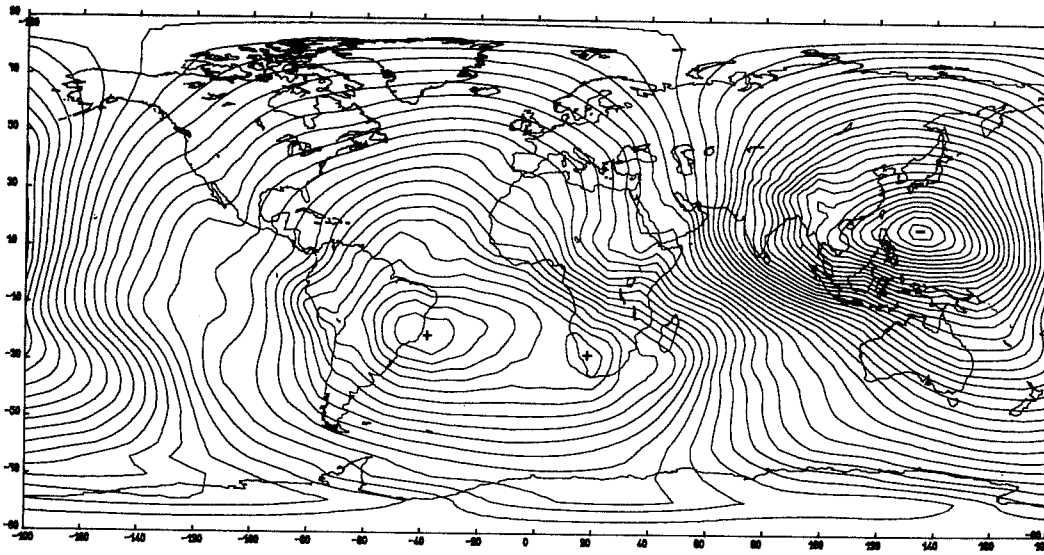

Fig. 20 Same as figure 19 but for July.

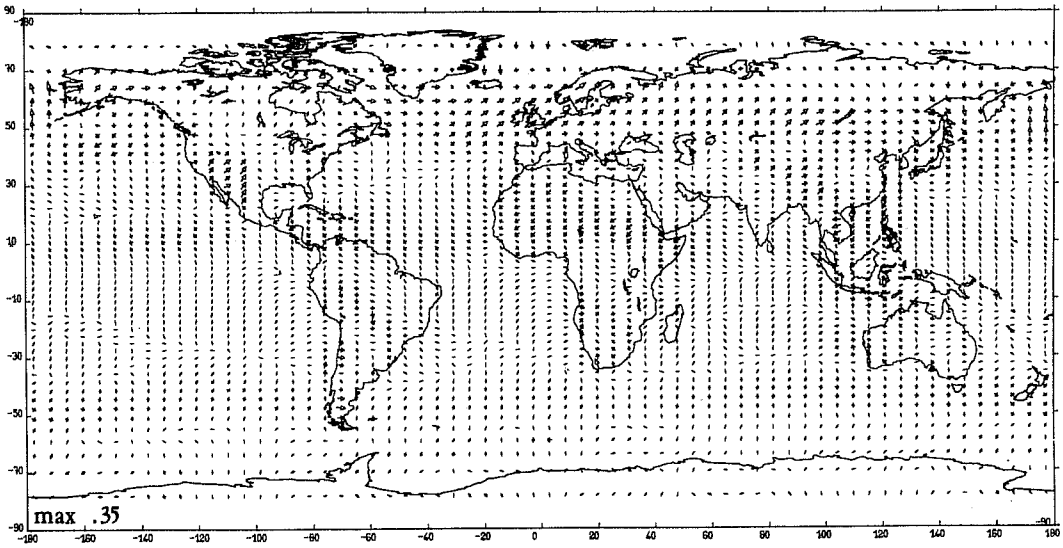

Fig. 21 Mean surface wind stress for January (in Pascals).

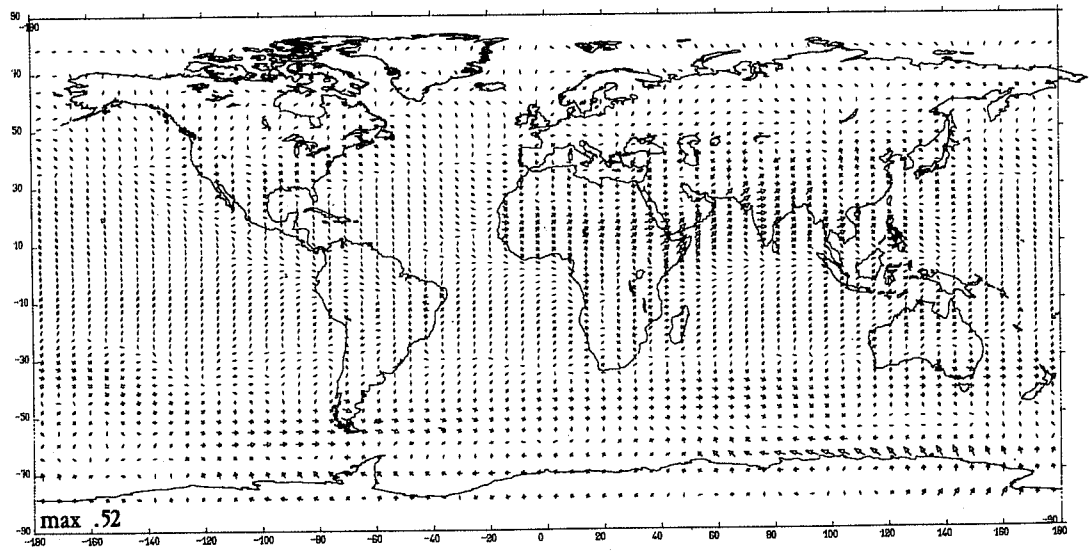

Fig. 22 Same as figure 21 but for July.

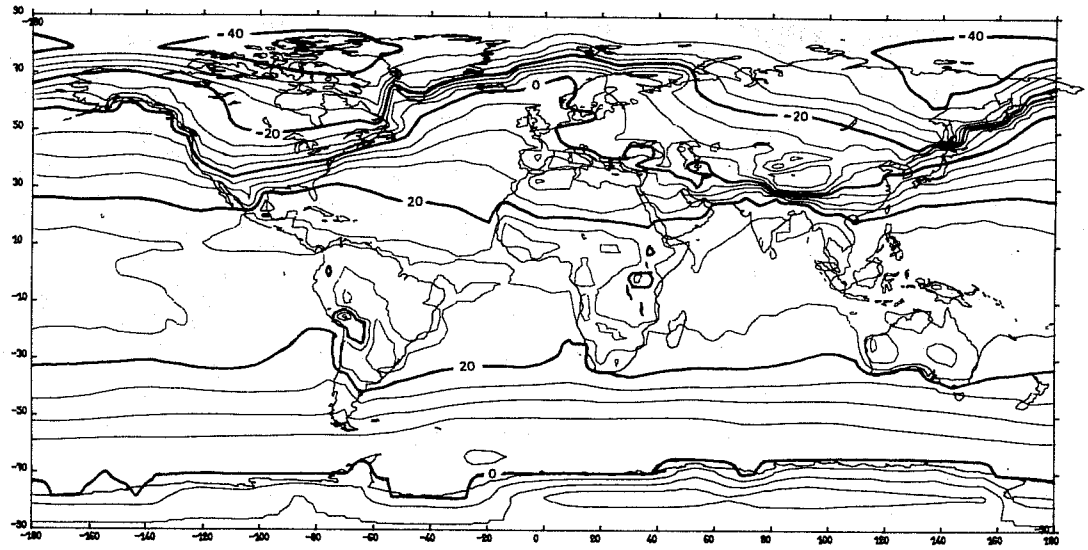

Fig. 23 Mean surface air temperature for January (in °C).

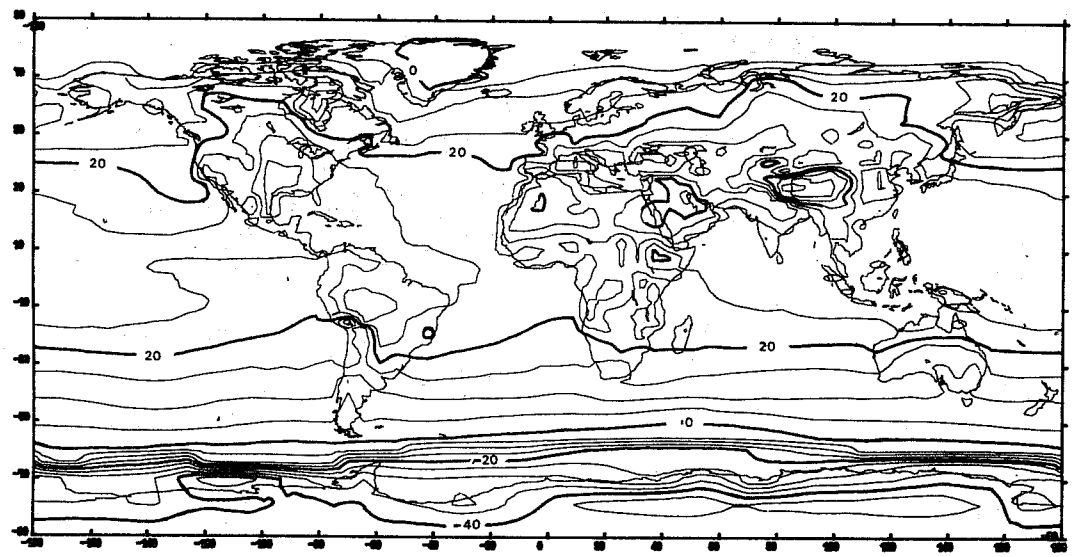

Fig. 24 Same as figure 23 but for July.

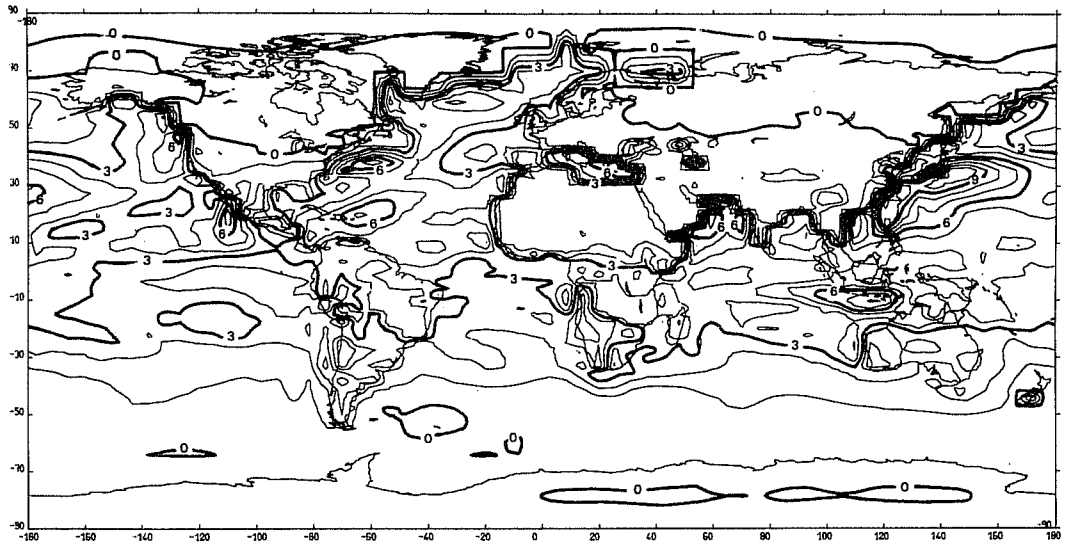

Fig. 25 Mean evaporation for January (in mm per day ; spacing : 1 mm per day).

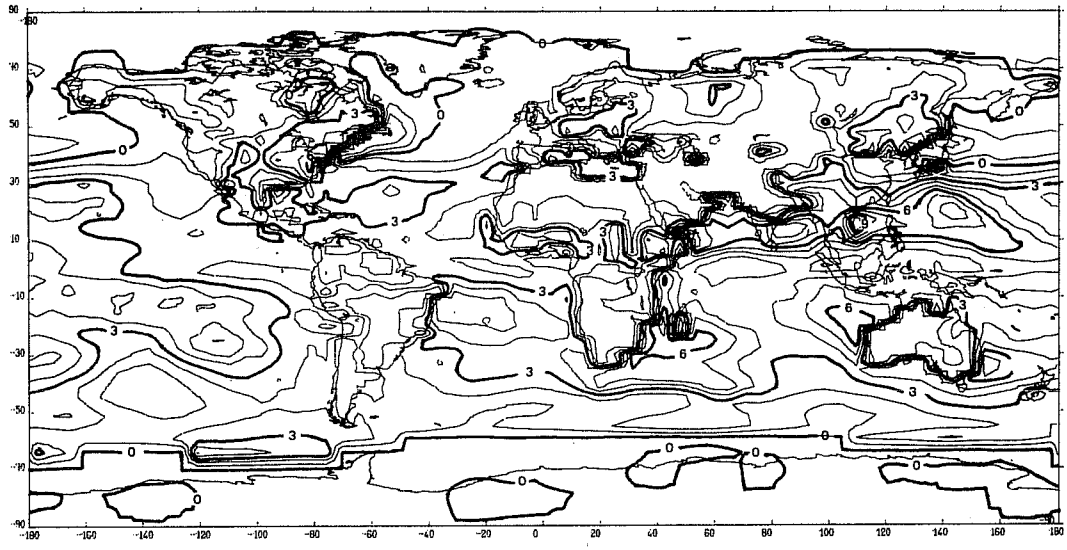

Fig. 26 Same as figure 25 but for July.

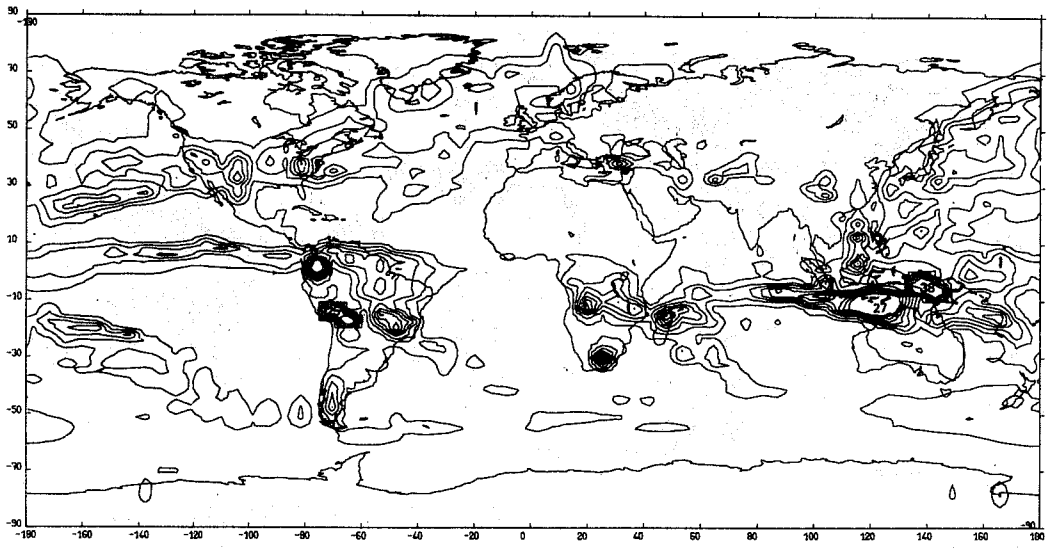

Fig. 27 Mean precipitation for January. Spacing : 2 mm day^{-1}.
No isoline above 16 mm day^{-1}.

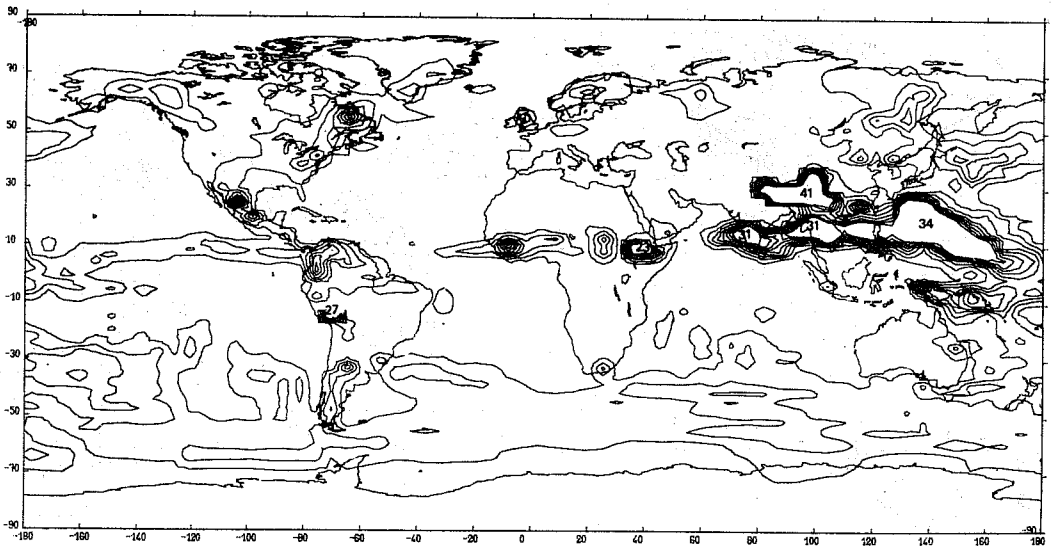

Fig. 28 Same as figure 27 but for July.

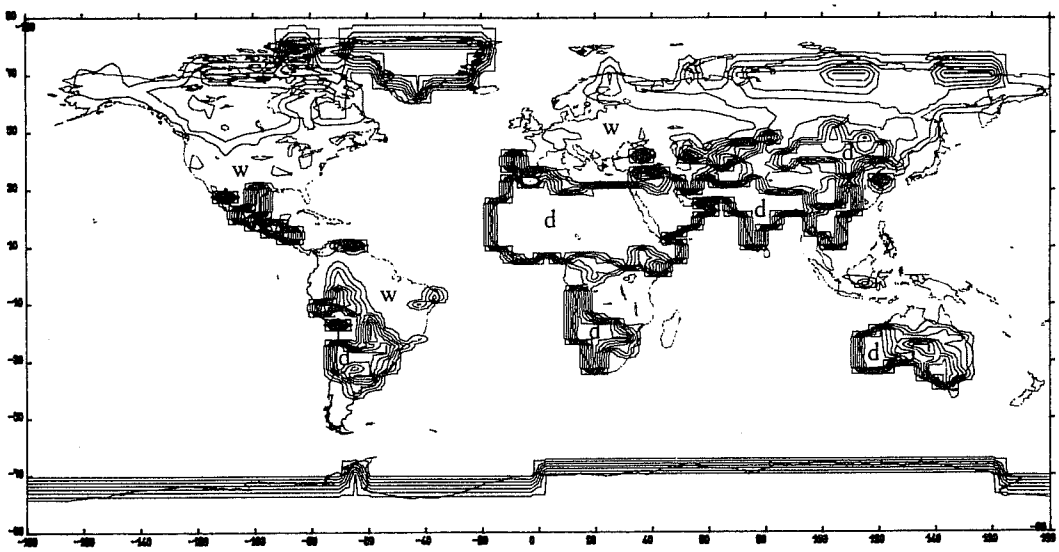

Fig. 29 Mean ground moisture for January (in percents of field capacity ; logarithmic spacing : 1,2,4, 8,16,32,64 per cent ; letter w indicates more than 64 % ; letter d indicates less than 1 %).

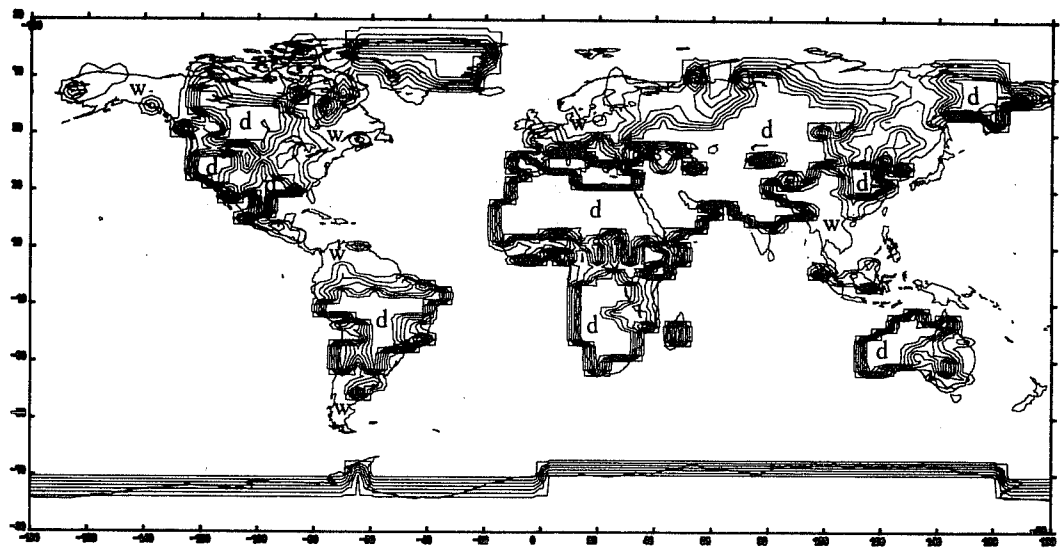

Fig. 30 Same as figure 29 but for July.

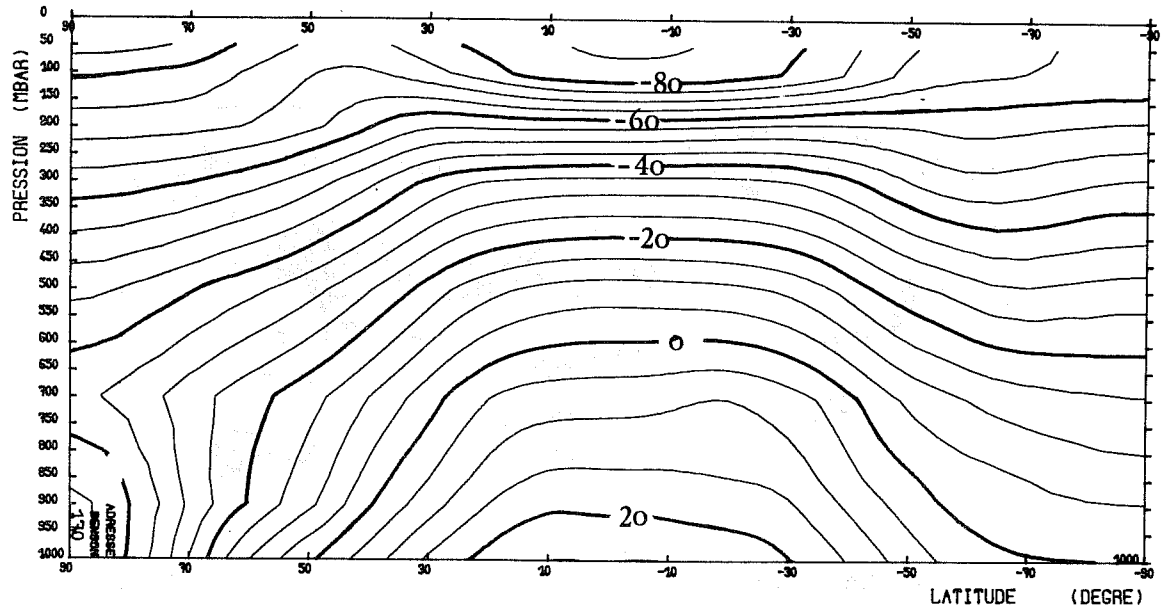

Fig. 31 Meridional cross section of monthly-and zonally-averaged temperature (in degrees C) for January.

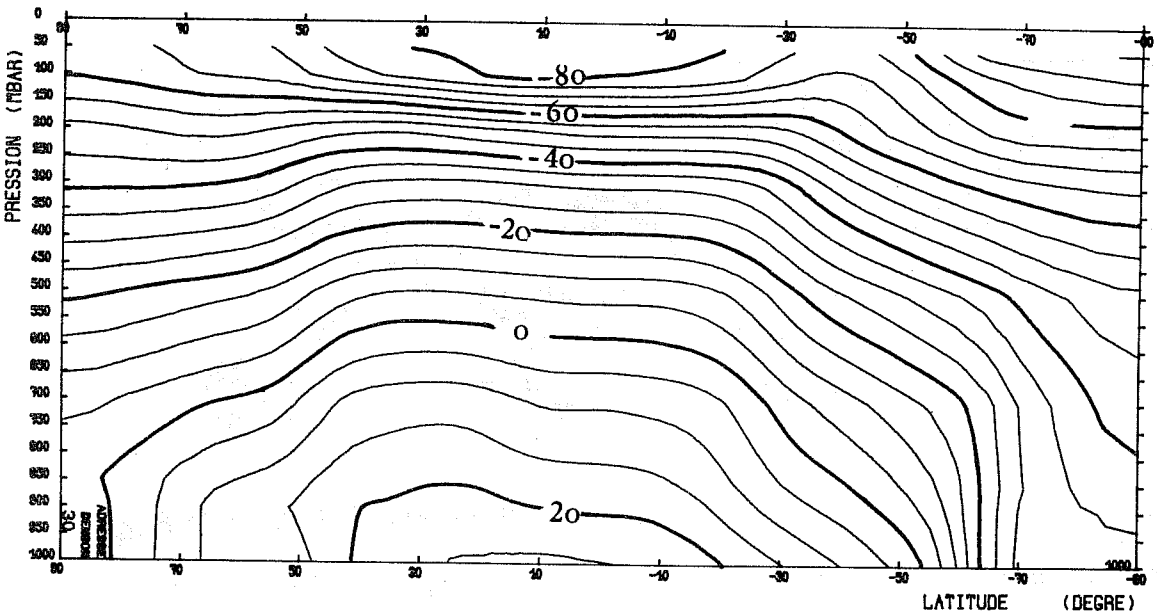

Fig. 32 Same as figure 31, but for July.

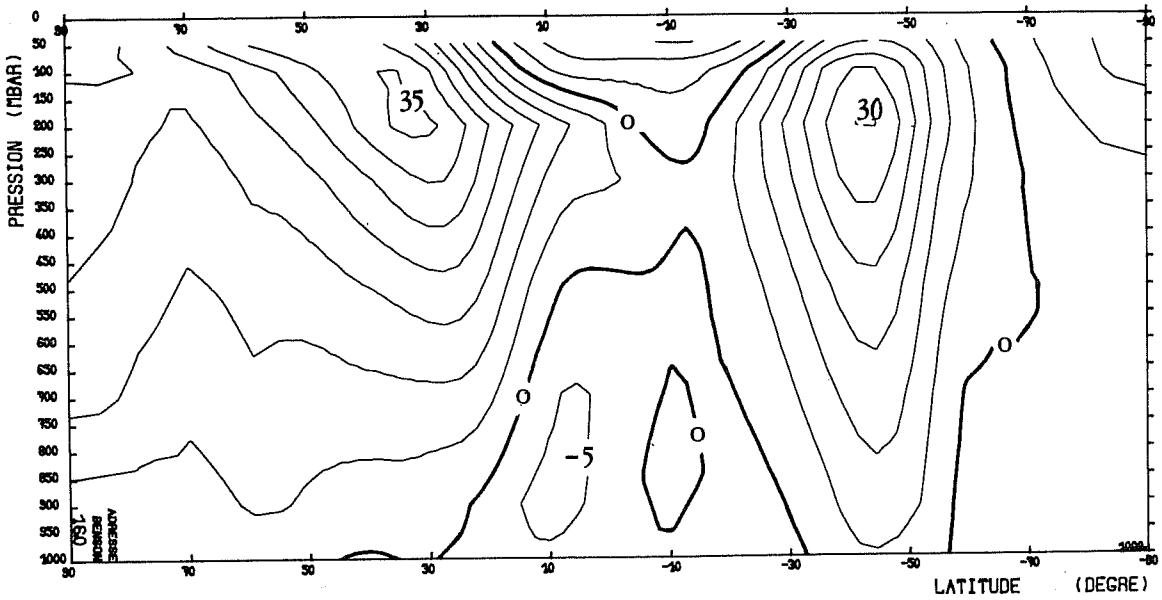

Fig. 33 Meridional cross section of monthly-and zonally-averaged zonal velocity (in m s^{-1}) for January.

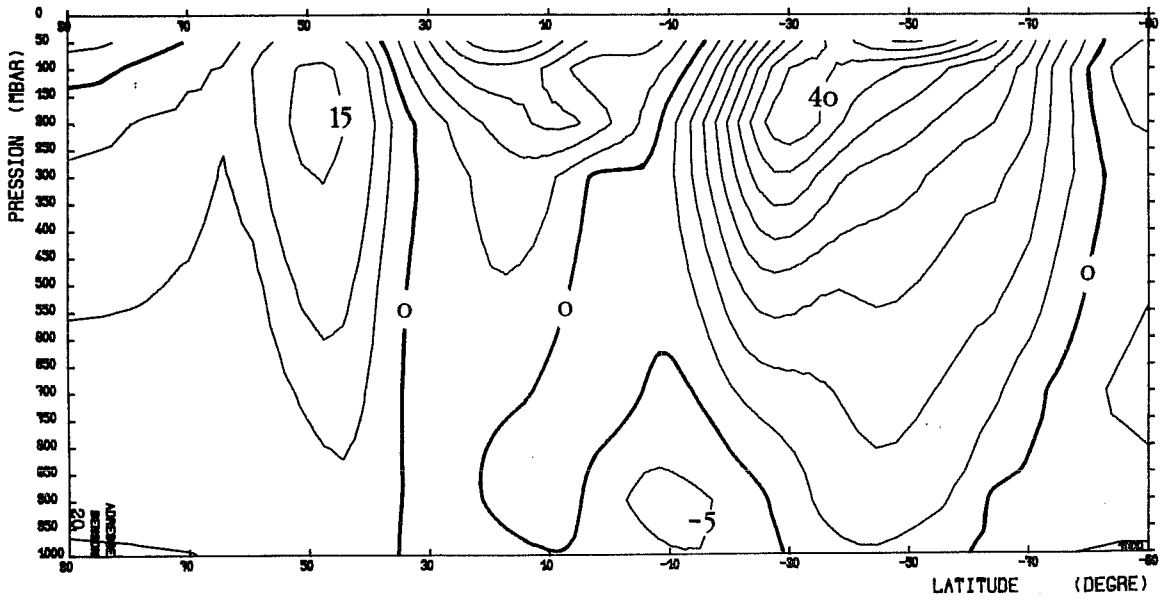

Fig. 34 Same as figure 33 but for July.

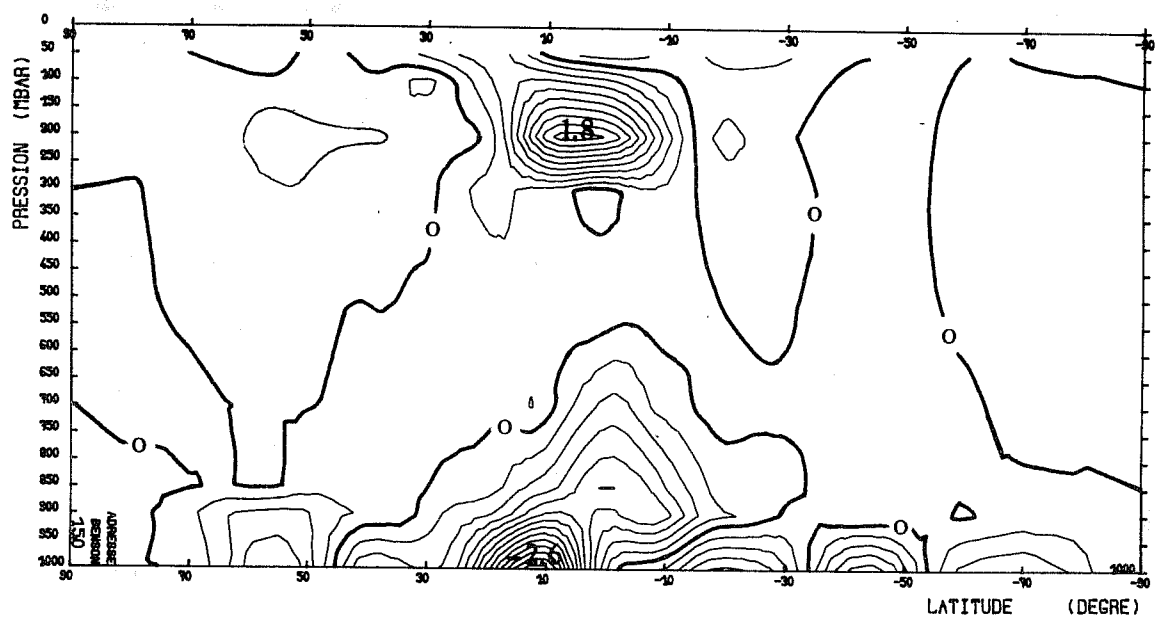

Fig. 35 Meridional cross section of monthly-and zonally-averaged meridional velocity (in m s^{-1}) for January.

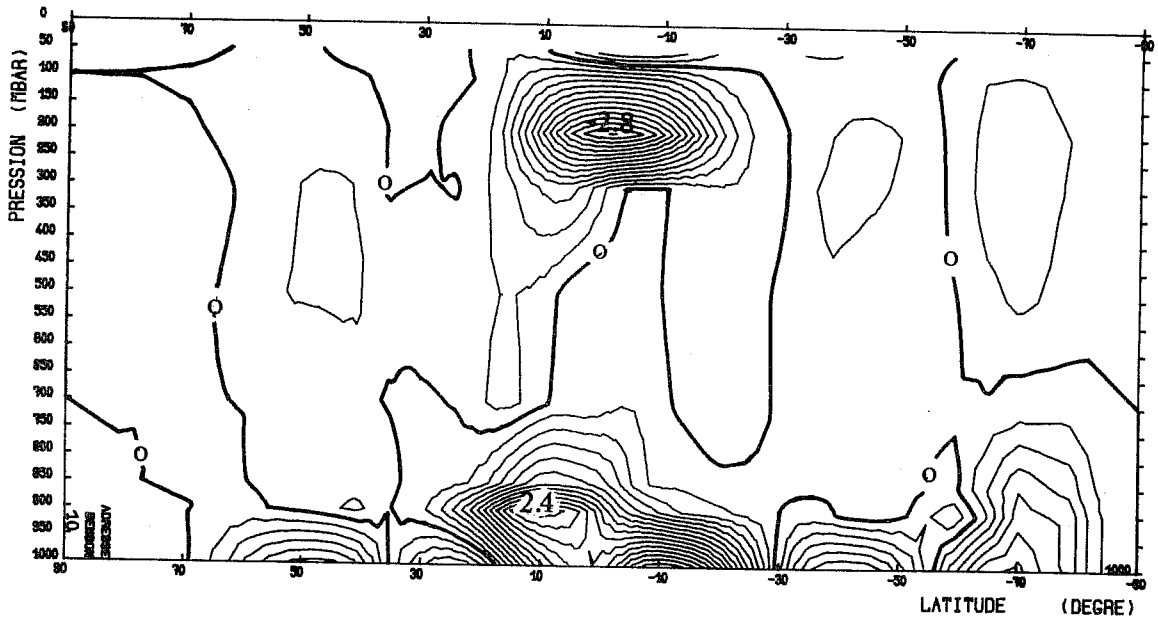

Fig. 36 Same as figure 35, but for July.